Detecting gas upwelling hazards in coastal areas through integration of active and passive electrical and seismic methods (Fiumicino, Central Italy)

Giorgio De Donno*[a], Alessandro Bosman[b], Ettore Cardarelli[a], Michele Cercato[a], Giuliano Milana[c], Guido Penta de Peppo[a]

[a] *"Sapienza" University of Rome - DICEA, Via Eudossiana 18, 00184 Rome, Italy*

[b] *Istituto di Geologia Ambientale e Geoingegneria (IGAG), Consiglio Nazionale delle Ricerche r.u. "Sapienza" University of Rome – DICEA*

[c] *Istituto Nazionale di Geofisica e Vulcanologia (INGV), Sezione Roma 1, Rome, Italy*

*corresponding author: giorgio.dedonno@uniroma1.it

DOI: https://doi.org/10.1016/j.enggeo.2023.107336

Abstract

The accurate location of gas upwelling flows is still an open problem for non-invasive imaging techniques in populated areas. Gas blowouts of deep origin may represent a serious threat to human health in urban areas and should be correctly imaged with high-resolution for assessing the related hazards. In this work, we propose an integration of active (electrical resistivity tomography and high-resolution sub-bottom profiling complemented with the multibeam bathymetry) and passive (self-potential and ambient noise recordings) geophysical methods to image gas upwelling flows in the coastal area of Fiumicino (Central Italy), where the gas presence is well-documented by previous works. We demonstrate that merging seismic sub-bottom profiling and electrical resistivity tomography has enormous diagnostic potential for gas detection, since they combine the high resolution needed to correctly image the subsurface and the interfaces between different media with the high diagnostic capability of electrical methods to detect anomalies associated with the gas emissions. Passive seismic methods complement the analysis enabling an estimation of the shear-wave velocity through array measurements. Finally, the reconstruction of the natural electrical sources, inferred from the inversion of self-

potential data, confirms the location of the near-surface gas upwelling flows assessed through the resistivity model. This work demonstrates that the integration of high-resolution active and passive seismic and electrical methods can be an effective choice for the accurate location of risk-prone areas by imaging the near surface gas pathways where borehole drilling is strongly limited if not forbidden.

keywords: electrical resistivity tomography; high-resolution seismic data; ambient noise recordings; self-potential; gas migration; geological hazard

1. Introduction

During the last decades gas blowouts have represented a serious threat to human health in urban contexts or when planning future urbanization (Hansell and Oppenheimer, 2004). Natural gases found in the shallow subsurface can have different causes, even if the most abundant are undoubtedly carbon dioxide (CO_2) and methane (CH_4). These gases are generally of deep origin and rise toward the surface through faults, cracks and voids, but may also be conveyed to the surface by borehole drilling (Barberi et al., 2007; Sella et al., 2014).

For these reasons, previous works have focused on locating gas in the shallow subsurface (e.g. Carcione et al., 2011), even if a standard procedure for identifying these gases through non-invasive investigations has not been established. In such geological scenarios where borehole drilling is limited, only a few geological data are available and non-destructive geophysical surveys are a cost-effective choice for imaging the gas pathways. Geoelectrical methods, such as electrical resistivity tomography (ERT), can be diagnostic for gas detection, as they can highlight the resistivity contrast between water-saturated (conductive) and gas-saturated (more resistive) media. In fact, the electric resistivity of porous sediments significantly increases when electrically conductive brine is displaced by CO_2 (e.g. Bergmann et al., 2012). However, a decrease of resistivity can be observed depending on the phase of the CO_2, in case dissolution in brine and uptake of dissolved solids occurs, although this effect is negligible for salinity between 20 and 160 g/l (Fleury and Deschamps, 2008), which is the range likely encountered in coastal areas. Examples of field application of ERT for gas detection are almost only restricted to monitoring CO_2 storage or injection experiments (Bergmann et al., 2012 and references therein) or to image hydrothermal upwelling fluids in large-scale surveys often located on volcanic areas (e.g. Gresse et al., 2017).

High-resolution (HR) seismic reflection profiles executed on land or in shallow water (rivers and channels) can complement and validate the electrical models, by inferring the subsoil layering down to significant depths as well as identifying the gas upwelling flows often visible on the seismic sections as blank zones of low-amplitude signal levels (e.g. Riedel et al., 2002). Furthermore, HR resolution multibeam bathymetry is often employed alongside seismic reflection for the morphological characterization of submerged areas and for pockmarks identification (Bosman and Orlando, 2017).

In recent years, the acquisition of passive seismic data has become routinary, due to the cost-effectiveness of this technique compared to active seismic surveys (Bard et al., 2004). Common applications of single-station recordings and array measurements include the detection of bedrock surfaces (e.g. Lane et al., 2008) and faults (e.g. Qian and Liu, 2020) rather than revealing degassing zones. However, low-frequency anomalies in spectral ratios of single-station microtremor measurements were observed in oil and gas fields in Austria (Lambert et al., 2009), even though their interpretation is still controversial.

Self-potential (SP) passive signals have been often recorded in volcanic areas, where a strong “W”-shaped signature (e.g. Barde-Cabusson et al., 2021) is often associated with upwelling flows and there are also some applications of SP to small-scale problems, where the magnitude of degassing phenomena is supposed to be much lower (e.g. Byrdina et al. 2009 and references therein; Nickschick et al., 2017). Additionally, some studies integrated SP with passive seismic methods as well as ERT for detection and monitoring of hydrothermal activities (e.g. Legaz et al., 2009).

In this work we present an integrated methodology that combines electrical and seismic methods to retrieve an accurate image of the gas upwelling flows and the geological features (gas reservoir, saline intrusion, stratigraphy) in coastal environments. The proposed approach is applied to the coastal area of Fiumicino prone to gas hazard as reported by many authors (see e.g. Carapezza et al. 2016) and located 25 km west of Rome (Italy), where we performed active (ERT and HR seismic sub-bottom profiler complemented with the multibeam bathymetry) and passive (ambient noise recordings and SP) investigations, to reduce the ambiguities often arising when geophysical techniques are applied standalone.

2. Study area and geophysical measurements

The study area is located on the Tiber delta in the Municipality of Fiumicino (Rome, Italy), close to the Fiumicino International Airport (Fig. 1) and to the coastline. Four areas were investigated in a narrow range of 5 km up to a maximum of 80 m depths from the coast to the Tiber River (Fig. 1). The near-surface layering, inferred from scattered borehole data, consists of three main geological units (Fig. 2), separated by unconformity surfaces (Milli et al., 2013), from the bottom to the top: i) clay and silty clay of Lower Pleistocene, belonging to the Monte Mario Sequence (MMS), ii) gravels and sandy gravels of the Middle Pleistocene Ponte Galeria sequence (PGS), iii) clay and peaty clay of the Upper Pleistocene to Holocene Tiber Depositional sequence (TDS).

The PGS formation is the most permeable layer hosting a ground aquifer where gas rising from depth may accumulate (Fig. 2). Conversely, the uppermost clays (TDS) act as an impervious cap rock for PGS gravels allowing gas pressurization (Carapezza et al., 2015).

Previous investigations in the study area included boreholes (Milli et al., 2013; Sella et al., 2014) and soil gas surveys (Bigi et al., 2014; Ciotoli et al., 2016; Maffucci et al., 2022), as well as a low-resolution multichannel seismic refraction profile along the Tiber River (Bigi et al., 2014). PGS unit was found in these boreholes between 37.5 and 53 m below sea level (b.s.l.), although with significant variations of both depth and thickness throughout the study area (Table 1).

The maximum gas concentrations (CO_2 and CH_4) were found at two selected areas (Fig. 1): "Coccia di Morto" (Site 1), where the main degassing vent (Fiumicino Gas Vent) occurred in 2013 and near "Capo due Rami" (Site 2), on the right bank of the river, where the soil gas surveys recorded the maximum concentrations (Bigi et al., 2014; Ciotoli et al., 2016; Maffucci et al., 2022).

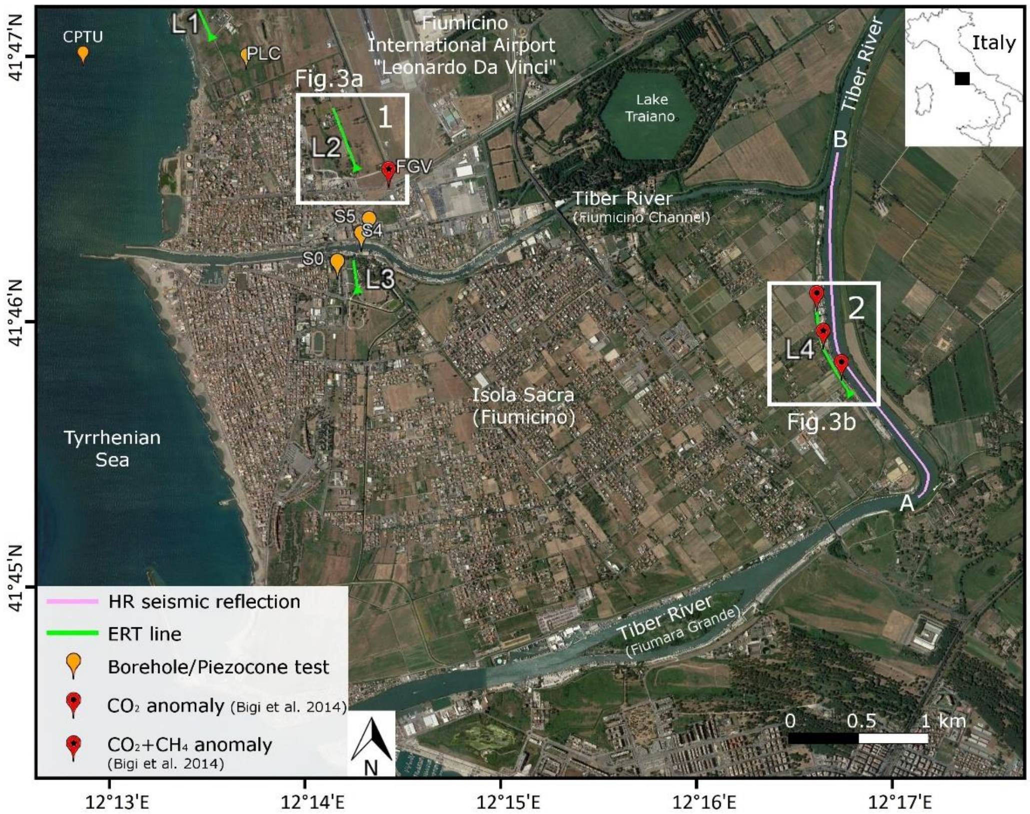

Figure 1. *Satellite image of the surveyed areas and location of the geophysical investigations with available boreholes and anomalous gas emission points after Bigi et al. (2014). The two*

main investigated sites, located at "Coccia di Morto" (Site 1, enlarged view in Fig. 3a) and near "Capo due Rami" (Site 2, enlarged view in Fig. 3b) are within white rectangles.

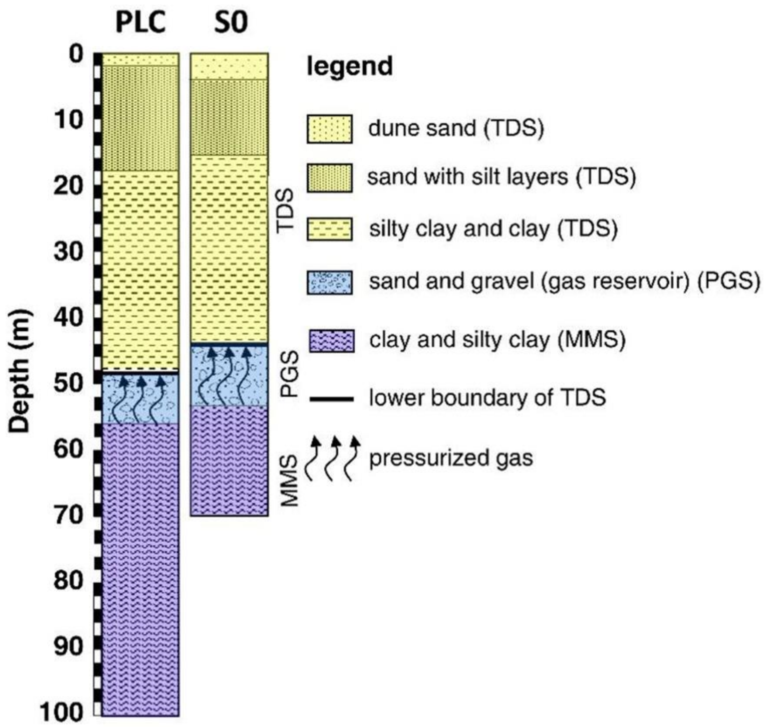

Figure 2. *Simplified stratigraphic column of deepest boreholes close to the investigated area: Pesce Luna Core (PLC, Milli et al. 2013) on the left and S0 (Sella et al. 2014) on the right. TDS: Tiber Depositional Sequence (yellow), PGS: Ponte Galeria Sequence (light blue), MMS: Monte Mario Sequence (purple). See Figure 1 for borehole locations.*

Borehole/ Piezocone test	**Elevation (wellhead)* (m a.s.l.)**	**Gravel roof (m a.s.l.)**	**Gravel bed (m a.s.l.)**
PLC[a]	1.0	-48	-53
CPTU[b]	-6.5	-37.5**	not found
S0[c]	1.8	-42	-52
S4[c]	1.8	-40	-47
S5[c]	1.3	-40.5	-50.5

Table 1. Location of gravel layer (PGS) from a piezocone test (CPTU) and boreholes: a. Milli et al. 2013, b. Technical report (private communication), c. Sella et al. 2014. All depths are

*referred to the sea level. *Orthometric elevation of the wellhead inferred from Laser Imaging Detection and Ranging (mesh 0.5 m) provided by the Italian Ministry of the Environment. **Value inferred from piezocone test results: tip resistance ~ 18 MPa and pore pressure > 600 kPa. See Figure 1 for borehole locations.*

We carried out preliminary geoelectrical investigations along two profiles (L1 and L3), almost parallel to the central Tyrrhenian shoreline (Fig. 1) and close to the available boreholes (PLC, SO and S4) and reasonably far from the known gas anomalies from previous measurements (e.g. Bigi et al., 2014). This initial survey aims to reconstruct the geological layering down to the TDS/PGS interface (depth of investigation - DOI ~ 45 m), the expected resistivity range of the geological formations and the location of the saltwater-freshwater interface, since the geoelectrical models can be validated by borehole data.

Then, we applied integrated geophysical surveys at the two selected sites (Site 1 and 2 in Fig. 1). For Site 1 (Fig. 3a) we carried out a 2D array of ambient noise recordings, together with a deeper ERT line (DOI ~ 80 m). In this site, gas emissions can be expected due to the closeness to the main degassing event, although not still systematically recorded by soil gas surveys. Therefore, we only integrate ERT and passive seismic data to improve the knowledge of deep geological layering.

Then, the fully integrated approach is applied at Site 2 (Fig. 3b), where gas concentrations were clearly highlighted from previous measurements (Bigi et al., 2014; Ciotoli et al., 2016; Maffucci et al., 2022). At Site 2, we take advantage of the high-resolution (HR) seismic reflection profile (purple line A-B in Fig. 1) acquired along the Tiber River (Fiumara Grande branch), together with a high-resolution multibeam bathymetry of the riverbed. The ERT data were acquired on a long (700 m) and deep (DOI ~ 80 m) profile (L4 in Fig. 3b) along the levee of the Tiber River. We also used passive geophysical methods (self-potential and ambient noise recordings) to complement the active methods thus reducing the uncertainty in the interpretation of geophysical models. Passive seismic measurements were carried out with a single-station technique, due to the limited space available on the levee.

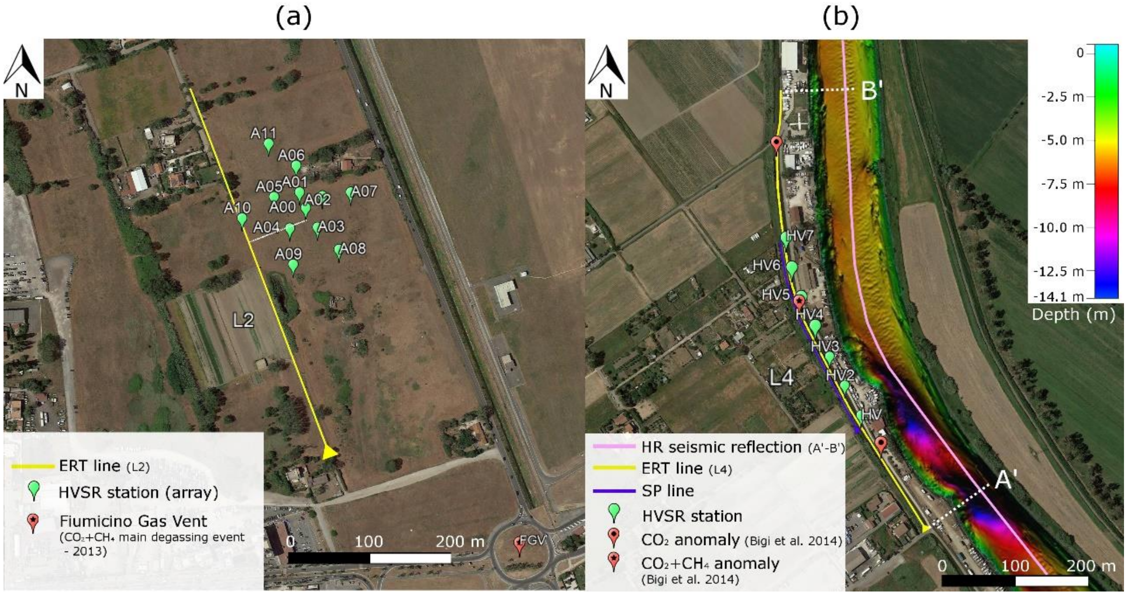

Figure 3. *Detail of the geophysical survey. (a) Site 1, (b) Site 2. The white line represents the projection of the array center to the L2 line. High-resolution multibeam bathymetry of the Tiber River is superimposed on the site map. The reader is referred to Figure 1 for the large-scale location of the investigated sites.*

3. Data acquisition, processing and inversion

3.1. Electrical Resistivity Tomography (ERT)

The ERT profiles were acquired using the IRIS Instruments Syscal Pro resistivimeter with 48 stainless steel electrodes spaced 5 m (L1 and L3 in Fig. 1) and 10 m (L2 and L4 in Figs. 3a and 3b respectively) apart, depending on the external limitations. Multiple gradient array is employed for ERT acquisition, using a maximum dipole length $a = 5$ and a maximum separation factor $s = 9$ (738 data points for each baseline), as it combines consistent signal strength in high conductive environments with good resolution and depth of investigation. For the L4 line, the ERT dataset was acquired using the roll-along technique by overlapping 40 electrodes for each baseline (240 new points for each new section and 100% coverage). We use a 12V - 110 Ah external battery for power supply recording satisfactory current levels (1-2.5 A) along the line, mainly due to the relatively low resistivity of the sediments because of closeness to the sea. Conversely, the extremely conductive environment leads to a low signal-to-noise ratio for the L1 line (executed on the shore), due to the low voltage drop recorded.

We filtered raw data for negative apparent resistivity values and for clear isolated points, but we decided to keep in the datasets also points with high percentage standard deviations. In fact, the percentage error fails to properly assess the reliability of a measurement for zero or close to zero observations (Sanders, 1997), such as those recorded in the highly conductive coastal environments where voltage drops are often very low. Consequently, we reported all errors in the following ERT models as both percentage and absolute values.

Apparent resistivity data were inverted using the VEMI algorithm (De Donno and Cardarelli, 2017), where the two-dimensional forward solution is achieved using a finite element approach with quadrangular elements, while a Gauss-Newton iterative formulation, based on the minimization of the l1-norm (the so-called robust or blocky inversion), is used for data inversion (Loke et al., 2003). The robust inversion is highly indicated for this case study since it is less sensitive to data points with larger errors and it can enhance the sharp transitions between different media (Loke et al., 2003). Although a priori information can be introduced into the inversion process using VEMI, we made no preliminary assumption on the soil layering.

3.2. Acoustic survey: HR seismic reflection sub-bottom profiling and multibeam bathymetry

The high-resolution (HR) seismic profiling was performed using a Benthos Chirp III source with a sweep between 2 and 7 kHz and a single-channel zero-offset configuration (Bosman and Orlando, 2017) on board a small vessel. GNSS positioning of the single-channel seismic was conducted in Real Time Kinematic (RTK) referred to as the “Mose” base station located at “Sapienza” University of Rome (permanent GNSS network, frame ETRF2000 epoch 2008). The baseline is approximately 22 km and provided a centimetric accuracy for this mono-channel seismic survey. Raw data were processed through Geo Suite All Works software, and we set for the time-depth conversion a value of 1470 m/s in water (measured in situ by a sound velocity profiler sensor) and 1550 m/s for the underlying sediment, estimated as a mean value for unconsolidated silty/clayey sediments at shallow depths (Hamilton, 1979). Although there are some recent attempts to filter out multiples e.g. through gapped deconvolution (Vesnaver et al., 2021), we prefer to only note them wherever occur in the acoustic record to avoid distortion of the seismic signals or attenuation of underlying weaker signals.

The HR bathymetry survey of the Tiber River was performed using the Teledyne Reson SeaBat 7125 echo-sounder (400 kHz) using the multibeam transducers in standard mode (look down) and rotating the head 30° to investigate the riverbanks up to hydrographic zero level. The vessel positioning was supplied in real-time by an Applanix Position and Attitude System (POS/MV wave master V5) using RTK corrections received by a GNSS master base station belonging to the GNSS National Dynamic Network (MOSE http://www.igmi.org/rdn/). Data were also re-processed with post-processing kinematic (PPK) techniques by means POSPac MMS software for very highly accurate positioning of the soundings. Multibeam bathymetry data were processed using Caris Hips & Sips 9.1 hydrographic software to generate a high-resolution Digital Elevation Model (DEM) with a 0.2 m cell size. The processing workflow consisted of replacing GNSS positions processed in PPK mode, sound velocity refraction editing, patch test, tide correction based on PPK GNSS/IMU data techniques and application of statistical and geometrical filters to remove coherent/incoherent noise (Bosman et al., 2015).

3.3. Ambient noise recordings

Site 1 was investigated by a 2D seismic array based on 12 standalone seismic stations equipped with a 3-component velocity sensor Lennartz LE3D-5s with an eigenfrequency of 0.2 Hz. Signals were continuously recorded during a 2-hour time window using a high-resolution 24-bit Reftek130 datalogger at a sampling rate of 250 samples/s. Array geometry was quite sparse with a maximum aperture of about 150 meters and a minimum spacing of about 18 meters. Stations were positioned using a GNSS Leica 1200 receiver (DGPS) to reduce the position errors to less than 5 cm.

Signals were processed using the open-source software Geopsy (Wathelet et al., 2020) to obtain Rayleigh waves ellipticity (horizontal-to-vertical spectral ratio - HVSR) and dispersion curves along with site resonance frequency (f_0). The HVSR data were analyzed following the guidelines and recommendations of the SESAME project (Bard et al., 2004). The dispersion curve was obtained by applying both conventional and high-resolution FK analysis (Capon, 1969; Ohrnberger et al., 2004) along with the Modified Spatial Autocorrelation (MSPAC) technique (Bettig et al., 2001) to extend the investigated frequency range toward the low-frequency band.

For Site 2 we used a three-component Sara seismic sensor with a natural period of 5 s; the duration of the seismic noise records was set to 45 minutes employing a sampling frequency of 100 Hz. Time alignment of samples and positioning were guaranteed by a GNSS receiver (DGPS). Also in this case we processed the ambient noise signals using Geopsy with the SESAME recommendations to obtain the HVSR curves and the resonance frequency (f_0), and to extract the directivity information of the signals by plotting the spectral ratio as a function of both frequency and azimuth. Data processing was performed with a 25 s time windows adopting the following processing parameters: short-term average (STA) = 1, long-term average (LTA) = 30, with min and max STA/LTA thresholds between 0.2 and 2.5. A 5% Tukey window function was applied to the raw signal and the curves were smoothed using the Konno and

Omachi (1998) method, with a smoothing constant of 40. Outlier curves are manually rejected from the software. For the computation, we used a frequency band from 0.4 to 20 Hz.

3.4. Self-potential

Self-potential (SP) data were acquired with an offset of 180 m to the first electrode of the L4 line (Fig. 3b), by a string of 10 non-polarizable electrodes ($Cu/CuSO_4$), spaced 5 m apart, rolled along the investigated profile by overlapping an electrode pair for each baseline. At each station, a small hole (~10 cm deep) was dug to improve the electrical contact between the electrode and the ground. The electrodes are connected to the Syscal Pro via the same equipment used for ERT survey. For each line, we performed from 5 to 10 repetitions every 2 minutes starting from 20 minutes after the electrode plug-in, to check the robustness and consistency of the measurements. SP data were filtered for outliers and inverted using the SP2DINV software (Souied Ahmed et al., 2013), achieving a current density model directly related to the underground sources. Data inversion was carried out using Tikhonov approach with a depth weighting matrix, computing the regularization parameter with the generalized cross-validation (GCV) method (e.g. Jardani et al., 2008).

4. Results

4.1. ERT preliminary survey

The ERT inverted models for the L1 and L3 lines are shown in Fig. 4a and Fig. 4b, respectively. In both cases, the electrode spacing is 5 m so that the ultra-shallow weathered layer is not imaged at all, and we can consider the water level coinciding with the ground surface. In one case (L1), the surface aquifer is salt water, whereas for the L3 line a fresh-water aquifer overlies salt water. The relatively high percentage error on L1 (14.3%) is due to the extremely low conductive environment (mean apparent resistivity ~ 1 Ωm) but is satisfactory if evaluated in absolute terms (~ 0.2 Ωm).

The L1 line (close to the coastline) detects a slightly resistive layer (3-5 Ωm) down to 5-7 m b.s.l., while resistivity decreases to 0.5-1.5 Ωm between 8 and 35 m b.s.l. This effect is almost only related to a lithology change between shallow dune sands and deeper clays and silts (both belonging to TDS) since the saltwater level is close to the surface (0 m a.s.l.). Then, we observed a slight resistivity increase in the gravel PGS formation (z > 35 m b.s.l.), which is known to host the gas reservoir, from borehole data in the adjacent CPTU (offshore) and PLC (Fig. 2). The depth of the reconstructed surface varies between 30 and 40 m along the investigated line, thus demonstrating the variability of the lower boundary of TDS already seen between CPTU and PLC (Table 1). ERT models do not show significant effects of gas upwelling since resistivity remains approximately constant within the silt/clay layer (Fig. 4a). A similar layering is also reconstructed for the L3 line (1.5 km far from the seashore), although the first layer is thicker (0-8 m) and more resistive (8-30 Ωm). In fact, here the shallow ERT layering mainly reflects changes in water salinity rather than in lithology, since the distance from the seashore increased. The freshwater-saltwater interface is found at 8 m b.s.l. and the ERT model detects the gravel roof at 35-40 m, where resistivity increase (~ 5 Ωm) is likely due to gas saturation within the gravel layer (Fig. 4b).

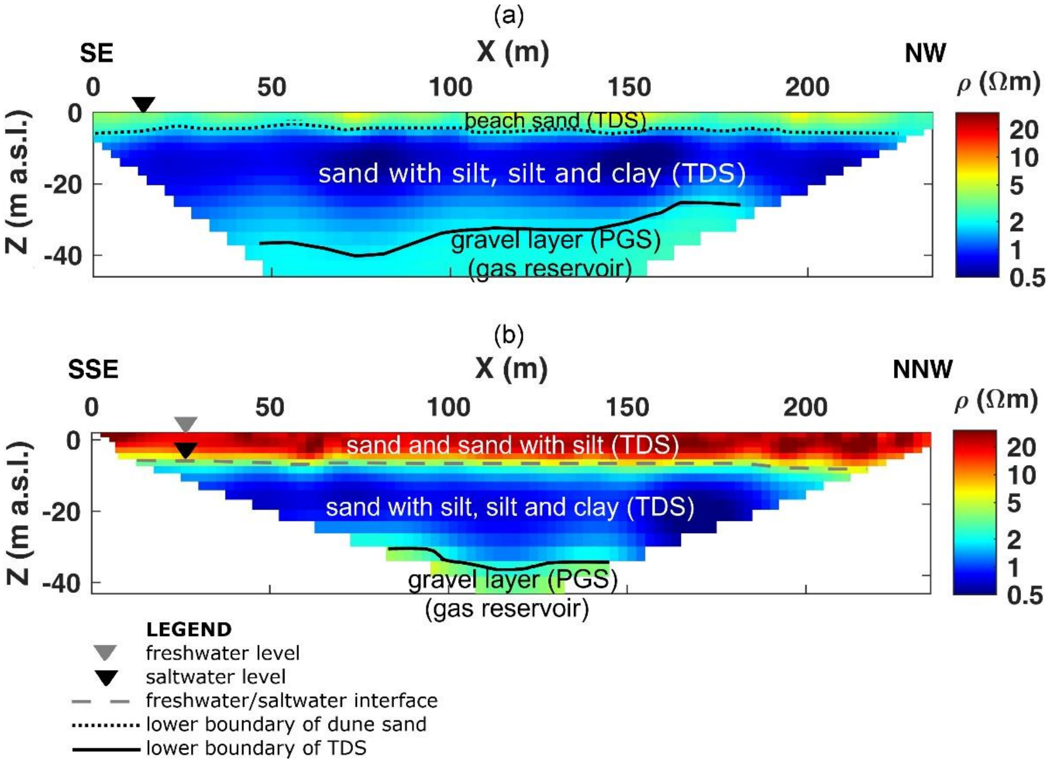

Figure 4. *Resistivity model for L1 (a). Error (AE): 14.3% (0.2 Ωm). Resistivity model for L3 (b) Absolute Error (AE): 5.9% (0.2 Ωm). TDS: Tiber Depositional Sequence, PGS: Ponte Galeria Sequence. See Figure 1 for location.*

4.2. Site 1

4.2.1. ERT

The inverted model of the L2 line (Fig. 5) with electrodes spaced 10 m apart, reached deeper zones (DOI ~ 80 m). The electrical layering is similar to the L3 model (Fig. 4b), even though the shallow resistive layer extends down to 15 m b.s.l.. Here the resistivity abruptly decreases to 0.5-1.5 Ωm between 15 and 55 m b.s.l., due to the presence of saline intrusion inland, while we observed a resistivity increase in the gravel PGS formation. A slight increase in the resistivity of the middle layer (ρ >1.5 Ωm, x = 210 and 310 m) can be likely attributed to the presence of gas upwelling flows if compared with the L1 and L3 models, where this effect is not visible.

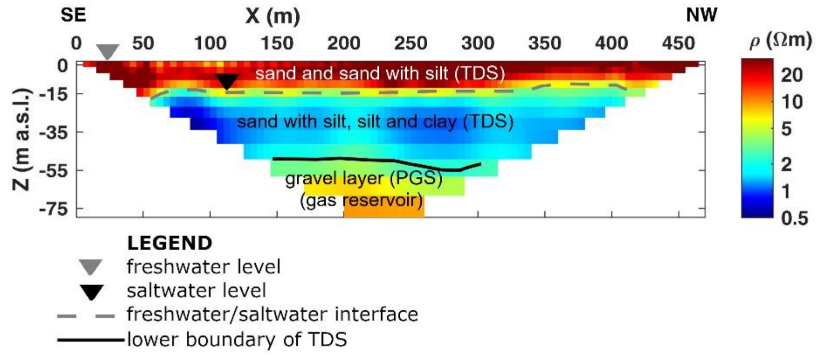

Figure 5. *Resistivity model for the L2 line (Site 1), where interfaces between different layers are marked with dotted lines. Absolute Error (AE): 18.8% (0.8 Ωm). Vertical exaggeration is 1.4. TDS: Tiber Depositional Sequence, PGS: Ponte Galeria Sequence. See figure 1 for location.*

4.2.2. Array measurements

HVSR data collected in the site 1 (Fig. 3a) show a complex behavior (Fig. 6a) with a peak at a very low frequency (0.2 Hz), very common in the Roman area (Marcucci et al., 2019) and a secondary one at about 1.5 Hz. These features are quite common at all recording sites. At frequencies higher than 3 Hz station’s behavior is no longer homogeneous suggesting some lateral variation in the velocity properties of the very shallow soil layers.

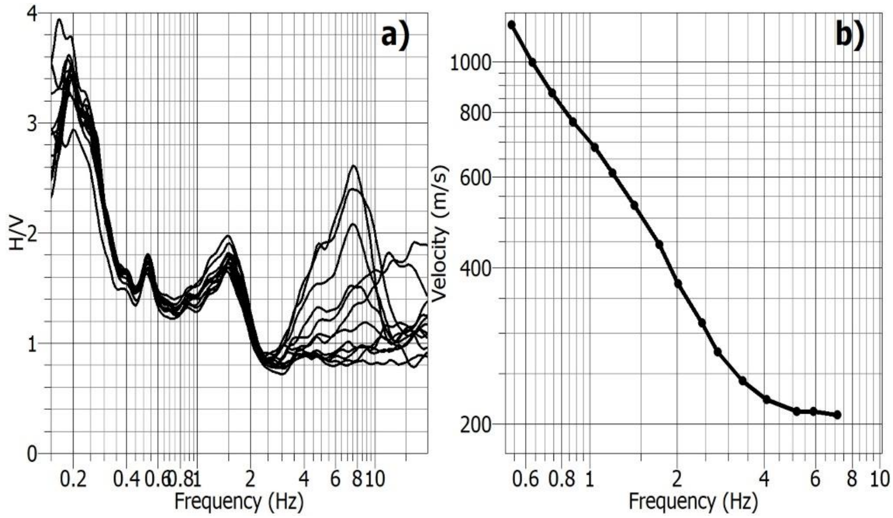

Figure 6. a) *H/V ratio for all the 2D array stations; b) Rayleigh fundamental mode dispersion curve obtained from the array data.*

The dispersion curve (Fig. 6b) is well-defined in the 0.55-7.5 frequency range. Due to the last observation and the large array aperture, it was not possible to retrieve information at higher frequencies. The good stability of data in the 1-3 Hz frequency range and the range of depth to be investigated suggest using this part of the ellipticity curve to be jointly inverted with the dispersion curve to obtain the shear-wave velocity (Vs) profile at the investigated site. The inversion was performed using again the Geopsy software package based on the Conditional Neighbourhood Algorithm (Wathelet, 2008; Wathelet et al., 2008). The fit of the inversion and the Vs model are shown in Fig. 7, where the ellipticity curve is calculated in terms of the arctangent, expressed in degrees, of the H/V spectral ratio. The dispersion curve is associated to the fundamental mode of Rayleigh waves. The initial model used in the inversion process was based on the results of the PLC borehole (Fig. 2). The inverted velocity models are represented at a maximum depth of 80 m since near surface characterization is the focus of this study.

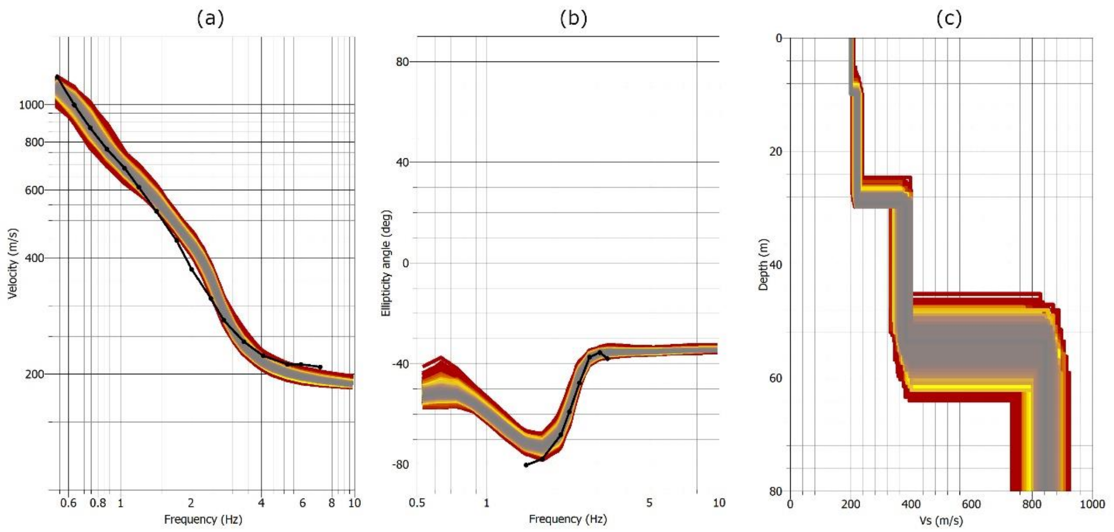

Figure 7. (a) *Fit of experimental (black line) and inverted ellipticity curve; (b) fit of experimental (black line) and inverted dispersion curve; (c) inverted Vs velocity model.*

The shear-wave velocity model (Fig. 7c) shows a low-velocity shallow layer (Vs between 200 and 250 m/s) with a first interface at depth of about 25 m where the velocity increases to 350-400 m/s. A major impedance contrast is found at depths between 50 and 60 m where Vs reaches the value of 800 m/s, likely due to the presence of the gravel layer as indicated by ERT.

4.3. Site 2

4.3.1. HR seismic reflection

The HR seismic profile A-B collected along the Tiber River (Fig. 8a), highlights two main reflections characterized by sharp bottom echoes, due to the riverbed (red line in Fig. 8b) and the unconformity articulated surface (green line in Fig. 8b) between TDS finer sediments and PGS gravels (estimated depth = 40-65 m along the profile) together with several blank zones, likely associated with accumulations of trapped gas. Conversely, there are no pieces of evidence of major faults along the investigated A-B section, as well as on the riverbed (Fig. 8a) since hyperbolas and/or layer discontinuities are not visible on the HR profile. Although the riverbed is characterized by bedforms (Figs. 3b and 8c), the HR multibeam bathymetry does not show the presence of faults or steps on the bottom of the river. However, it highlights the presence of depressed morphologies caused by localized erosion due to the hydraulic narrowing of anthropogenic features along the levees (parking spaces for cars), commonly found in this area of the Tiber River.

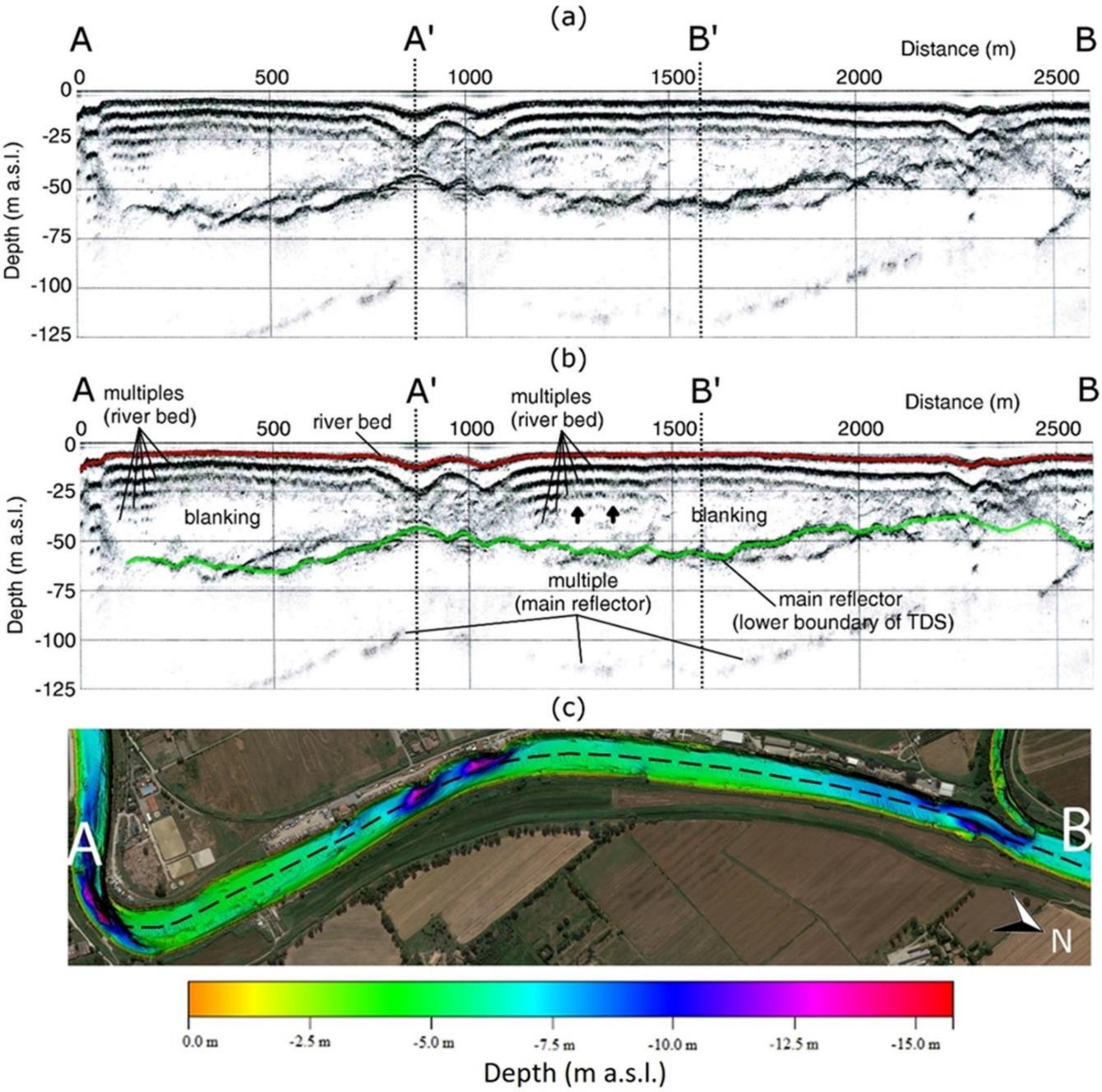

Figure 8. *(a) HR seismic sub-bottom profile A-B collected on the Tiber River. Alongside the A'-B' branch, electrical and passive seismic measurements were performed on land. (b) Interpretation of the profile A-B: red solid line – riverbed; green solid line – main reflector. Black arrows indicate the gas accumulation zone which corresponds to the blanking areas in the A'-B' branch. See Figure 1 for location. (c) HR resolution multibeam bathymetry collected along the Tiber River shows bedforms and large depressions produced by anthropogenic hydraulic narrowing. Bathymetric vertical datum: multibeam data were collected in ellipsoid elevation and then transformed to orthometric elevation using the Italgeo2005 model.*

4.3.2. ERT

In Fig. 9, we show the ERT model of the L4 line (DOI ~ 80 m), executed along the levee (height ~ 5 m), where the presence of gas vents was well documented (Bigi et al., 2014). The electrical layering, already seen on L2 (Fig. 5) is confirmed also for the L4 line, with the location of the unconformity surface in agreement with the A'-B' seismic sub-bottom profile collected on Tiber River. We detect six anomalous zones, elongated in the vertical direction, likely due to gas upwelling flows, of which the most significant is located between 380 and 410 m.

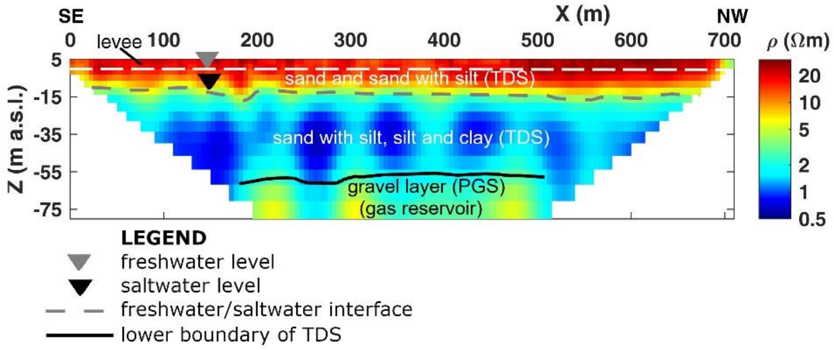

Figure 9. *Resistivity model for the L4 line (Site 2), where interfaces between different layers are marked with dotted lines. Absolute Error: 4.6% (0.3 Ωm). Vertical exaggeration is 2. TDS: Tiber Depositional Sequence, PGS: Ponte Galeria Sequence. See Figure 1 for location.*

4.3.3. Single-station ambient noise recordings

The H/V spectra for Site 2 (Fig. 10) exhibit only moderate amplification effects, as the maximum spectral ratio is around 2.1-2.2. The main resonant peak is located at 1.8-2.0 Hz for the first stations (Figs. 10a and 10b), even though it becomes less significant or barely visible for the last stations (Figs. 10c and 10d). This peak is likely associated to the seismic impedance contrast between the TDS finer sediments and the underlying gravels, as shown for the Site 1. For the last stations (HV5-7, Figs. 10c and 10d) a secondary peak at 4.5-5 Hz becomes prevalent, as well as a high-frequency response (10-15 Hz) is also observed for HV5. A clear effect of directionality is visible between 0-45°N and 160-180°N only for HV5 (Fig. 10g), while there are no significant effects on the other stations (Figs.10e, 10f and 10h).

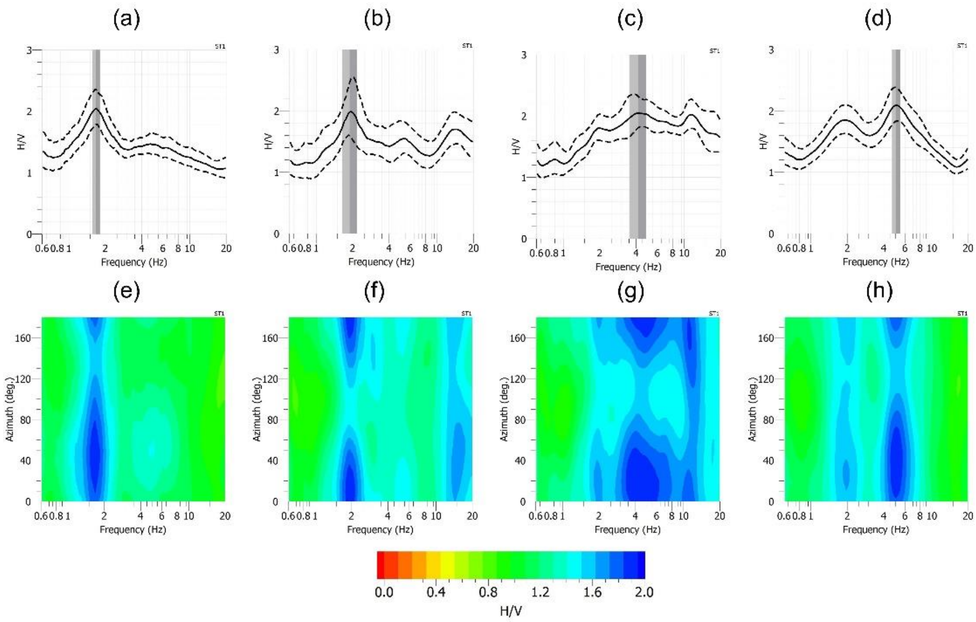

Figure 10. *Site 2: directionality of ambient noise recording for HV1 (a), HV3 (b), HV5 (c) and HV7 (d) stations (see Fig. 3 for the location of stations).*

4.3.4. Self-potential

Self-potential observed data are shown in Fig. 11a (gray line and circles) together with the fitting (predicted data) at the last iteration of the inversion process (black line). Although inversion fails to properly address some minor anomalies (i.e. x = 200-230 m), significant increases in current density between 290 m and 320 m and mostly between 360 and 420 m, are clearly highlighted, consistently with the resistivity anomalies shown by the ERT model. The maximum DOI is around 15 m (10 m b.s.l.), as proof that the SP method can enlighten in this case only the shallow portion of the subsurface.

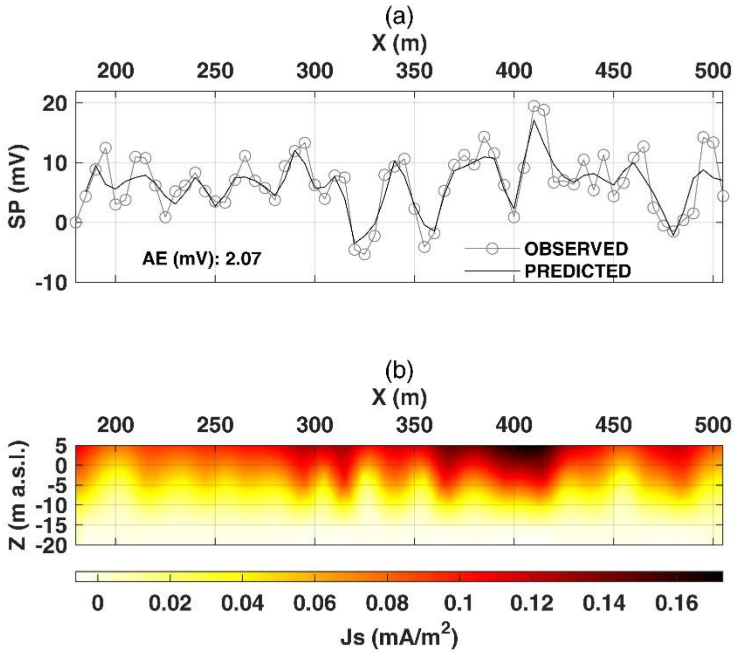

Figure 11. *Site 2: Inversion of SP data: (a) fitting between observed (grey line with open circles) and predicted (black line) data; (b) current density model.*

4.4. Data integration

Data integration for the two investigated sites is reported in Fig. 12. For Site 1 (Fig. 12a), the deep interface, associated to the transition between TDS (sand, silt and silty clay) and PGS (gravel layer) identified in the resistivity model of Fig. 5, is detected at approximately the same depth (~ 55 m b.s.l.) of the shear velocity profile reconstructed from inversion of array measurements (superimposed to the ERT model in Fig. 12a), where there is a strong seismic impedance contrast (approx. from 400 to 800 m/s), thus strengthening the validity of the proposed interpretation. Additionally, data integration confirmed that the interface at approximately 15 m b.s.l. is related to a transition between media having different salinity and not to a lithological change.

Also at Site 2, the integration of the HR seismic data and the ERT profile shows a good correspondence between the increase of resistivity due to the gas reservoir and the main reflector (depth ranging from 45 to 55 m b.s.l. along the investigated profile), with minor discrepancies in the left part of the section, likely due to the first-approximation value of velocity chosen for the time-depth conversion. The main resonant frequency of single-station recordings is 1.8-2 Hz, slightly higher than that retrieved by the array measurements, likely due to the shallower position of the TDS/PGS interface compared to Site 1 (50-60 m) or to minor lithological changes between the two sites. The resistivity model highlights six main gas plumes upwelling from the reservoir (black arrows), defined as the lower boundary of TDS. Three of these (located approx. at 300, 400 and 480 m) match exactly the current density increases in the SP model, even though this evidence is limited to the shallow portion of the subsurface. The main anomaly is located approx. at x = 400 m, also validated by surface gas measurements made by previous works (Bigi et al., 2014; Ciotoli et al., 2016), highlighting both CO_2 and CH_4 emissions at this position. Additionally, the station which shows a clear directional effect (HV5) is located where active and passive electrical methods show the presence of the most significant gas rise.

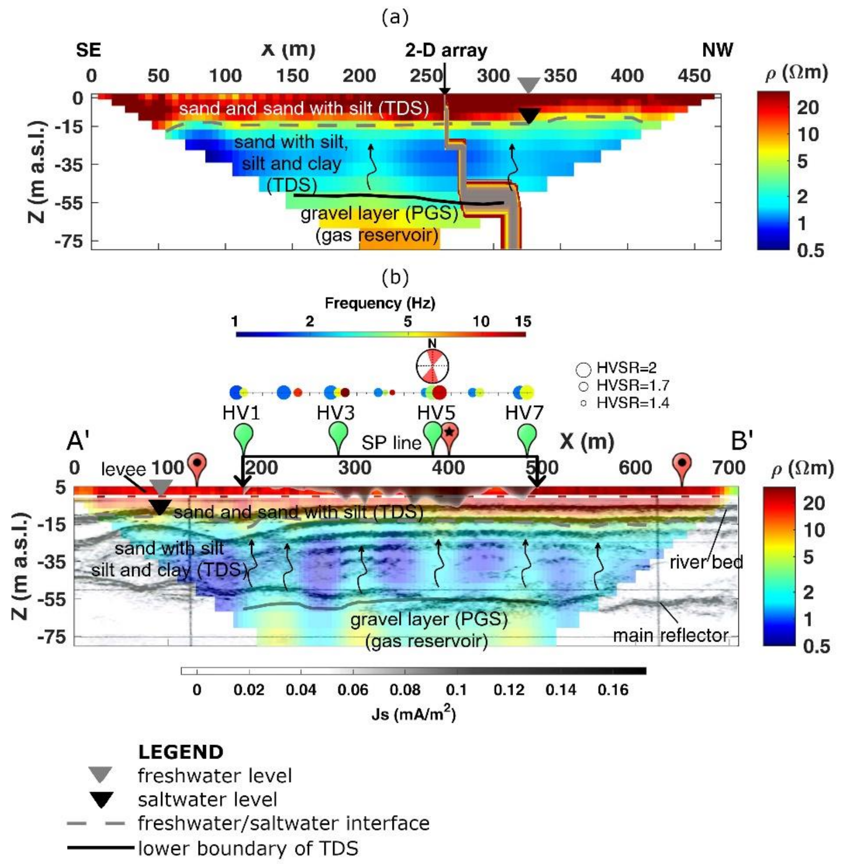

Figure 12. *Data integration at (a) Site 1 and (b) Site 2 where imaged gas upwelling flows are marked with black arrows. Site 1: resistivity model for the L2 line (Fig. 5), where the Vs model from inversion of array measurements is superimposed. Site 2: resistivity model for the L4 line (Fig. 9), where HR seismic sub-bottom profile A'-B' and current density model (only values > 0.05 mA/m²) are superimposed. ERT and HR seismic profiles are spaced 90 m apart on average. The dashed white line indicates the bottom of the embankment. Green pins indicate HVSR stations, while red pins indicate CO_2 (black-filled circles) and CO_2+CH_4 (black-filled star) anomalies after Bigi et al. (2014). TDS: Tiber Depositional Sequence, PGS: Ponte Galeria Sequence.*

5. Discussion

Gas detection using geophysical investigation is a relatively new research topic if restricted to near-surface low emissions in urban areas, while extended literature is available for imaging of deep gas emissions in natural scenarios (Barde-Cabusson et al., 2021). In this context, drilling boreholes is strictly limited if not forbidden due to the risk of explosion of flammable gases and expensive operating procedures that have to be implemented when drilling. Therefore, surface geophysical methods, together with geochemical data are the only option to image the gas upwelling flows. In this respect a large preliminary screening performed with geochemical measurements, already examined in previous works for the Fiumicino area (Bigi et al., 2014; Ciotoli et al., 2016; Maffucci et al., 2022), is the best option to highlight the risk-prone areas and to focus the geophysical survey on selected areas, thus improving the cost-effectiveness on the whole survey. Despite the extreme environmental conditions encountered in this study ($\rho <$ 1 Ωm for large areas), the ERT method has been demonstrated to be effective and highly diagnostic for imaging gas upwelling flows, where resistivity approximately doubles compared to the neighboring zones (Fig. 12).

The geophysical investigation proposed in this work, where ERT is complemented by ambient noise recordings, SP and HR sub-bottom profiling, could be effectively employed for quantitative hazard assessment at a local scale, providing adequate resolution for moderate depth targets (maximum DOI in this case ~ 80 m). In Table 1 we summarized the main targets theoretically achievable by the proposed methods, with the limitations discussed below.

Method	Gas upwelling flows	Reservoir location	Near-surface geology	Saline intrusion
ERT	✓	✓	✓	✓
Sub-bottom profiling	✓	✓	✓	✗
Ambient noise (array)	✗	✓	✓	✗
SP	✓	✗	✗	✗

Table 2. *Main targets theoretically achievable by the proposed methods for gas-prone areas in coastal environments. ✓: detectable, ✗: not detectable.*

The loss of resolution with depth, intrinsic to the ERT method, can be mitigated by using HR seismic reflection methods in shallow water, since for deep zones the location of a resistive target cannot be evaluated accurately by ERT standalone, and deviations of some meters are common (e.g. Cardarelli and De Donno, 2017). Additionally, a high resistive anomaly (gas reservoir) might be reconstructed in the bottom pixels of the ERT model with lower resistivity values compared to those expected, due to the loss of resolution with depth (e.g. Gélis et al., 2010), as in this case where the resistivity increases only by few Ωm. For land surveys far from coastal areas or rivers, the HR single-channel seismic acquisition can be conveniently replaced by a multi-channel reflection, even with an increasing effort for data acquisition and processing and higher costs. Alternatively, ambient noise recordings could be a low-budget option to have a rough estimate of the reservoir depth, provided that the shear wave velocity is properly estimated by inversion of array data. Additionally, information about the presence of faults can also be inferred by the analysis of the signal directivity polarization of H/V spectra. Polarization transversal to the strike direction has been previously observed for normal and strike-slip faults, as a result of stiffness anisotropy in the fault zone (Pischiutta et al., 2017). In this case, the polarization as well as the blanking of seismic reflection signal observed in the high emission area can be used only as a general indication of anomalous zones, since their quantitative interpretation needs further theoretical and experimental investigations which are beyond the scope of this paper as well as the detection of the causes of degassing. In this regard, previous studies (Bigi et al., 2014; Maffucci et al., 2022) suggested that gas emissions are both natural and human-induced, since faults control the deeper fluid migration pathways, allowing the low permeability levels of the Lower Pleistocene to be supplied from depth, while human activities (primarily drilling) that cut the cover or reduce the lithostatic head, can allow the pressured gas to reach the surface.

Self-potential positive signals are strongly correlated to gas upwelling flows in volcanic areas (Zlotnicki and Nishida, 2003), even if with a higher magnitude compared to this case study where the maximum SP data is approximately 20 mV. Nevertheless, the SP level observed at the Fiumicino site is comparable to that recorded in similar terrestrial scenarios (Nickschick et al., 2017), where SP was also applied in combination with ERT. As in that case, anomalous SP zones are marked with fluctuating higher and lower magnitudes, similar to the W-shaped signatures observed for gas flows in volcanic environments (Barde-Cabusson et al., 2021). The current density model, reconstructed from the inversion of SP data, can delineate the gas accumulation in the shallow portion of the subsurface (DOI ~ 15 m), by complementing the ERT model. In fact, gas detection in the near surface through ERT can be biased by the increase of resistivity due to the decrease of salinity and/or saturation observed in the study area.

As an ancillary result, the ERT models also permitted an assessment of the freshwater (FW)-saltwater (SW) interface, even though only restricted to a few lines and with a lower resolution compared to that achievable with a high-resolution shallower survey only focused on SW detection. We chose a resistivity value around 3 Ωm as a threshold for locating the FW-SW interface, which was previously used for silty-clayey saturated sediments in similar coastal scenarios (e.g. Attwa et al., 2011; Goebel et al., 2017). In the north-western part of the study area, the position of the FW-SW was found approximately at 0 m b.s.l. for L1 (Fig. 4a, located 100 m far from the coastline), 15 m for L2 (Fig. 5, 1.1 km) and 8 m b.s.l. for L3 (Fig. 4b, 1.4 km). Therefore, the SW level is not only correlated to the distance from the coastline, but also to the hydrogeology (groundwater preferential pathways) and to anthropogenic causes (i.e. water abstraction for irrigation of the farms widespread in the study area) which can in turn favor the SW intrusion inland. The effect of hydrogeological and anthropogenic factors is magnified by the SW level (around 13 m b.s.l.) reconstructed for L4 line (located 3.6 km far from the coastline), which is comparable to those detected for L2 and L3 despite the increased distance from the sea. As a further confirmation of the latter result, similar SW levels, even if slightly shallower (8-10 m b.s.l.), were also found by a previous ERT survey in the adjacent Ostia Antica archaeological area (Cardarelli et al., 2017). These findings can pave the way for a future large-scale campaign focused on the assessment of the SW intrusion inland in the Fiumicino coastal area.

6. Conclusions

This work demonstrated the diagnostic potential of integrating active (ERT and HR sub-bottom seismic profiler with multibeam bathymetry) and passive (SP and HVSR) geophysical data for imaging gas emissions in coastal environments, like the one encountered in the Fiumicino area, where borehole drilling is strongly limited if not forbidden. The seismic sub-bottom profile in the Tiber River complemented with the multibeam bathymetry, gives an HR image of the subsurface down to a depth of ~ 60 m, locating the unconformity surface between Pleistocene/Holocene clayey sediments and PGS gravels and highlighting several blank zones likely associated with the gas emissions.

Through the combination of ERT (DOI ~ 80 m) and SP (DOI ~ 15 m) methods on a selected site, we reconstructed a three-layer model, where local increases in resistivity in the middle clayey layer are related to upwelling gas flows from the underlying gravel layer (gas reservoir). The analysis of ambient noise recordings highlights the seismic impedance contrast between the TDS finer sediments and the underlying gravels, while a clear directional effect is seen nearby the main gas emissions.

The integration of these methodologies also provides a more accurate reconstruction of the distribution of gases in the shallow subsurface down to 80 m, highlighting six main points of ascent. This indirectly also provides important information for risk assessment, which represents a critical issue in the management of urban areas, suggesting new elements to evaluate hazards in these zones.

Acknowledgments

This work was founded by “Sapienza” University of Rome, Grant no. 171/D/2016 and INGV, Grant. 961 - Principal Investigators: Ettore Cardarelli (2016-18) and Giorgio De Donno (2019-22). The authors wish to thank Francesco Pugliese (“Sapienza” University of Rome) and MSc and BSc students Francesco Giaconi and Michele Tomassetti (“Sapienza” University of Rome) for their help during field acquisition.

Data availability statement

The data that support the findings of this study are available from the corresponding author upon reasonable request.

References

Attwa M., Günther T., Grinat M., Binot F. (2011). Evaluation of DC, FDEM and IP resistivity methods for imaging perched saltwater and a shallow channel within coastal tidal flat sediments. J. Appl. Geophys. 75(4), 656-670.

Barberi F., Carapezza M.L., Ranaldi M., Tarchini L. (2007). Gas blowout from shallow boreholes at Fiumicino (Rome): Induced hazard and evidence of deep CO2 degassing on the Tyrrhenian margin of Central Italy. Journal of Volcanology and Geothermal Research, Vol.165, Issues 1–2, 15 August 2007, Pages 17-31.

Bard P.Y. and the SESAME Team. (2004). Guidelines for the implementation of the h/v spectral ratio technique on ambient vibrations measurements, processing and interpretation.

SESAME European research project EVG1-CT-2000-00026 , 1–62, available at: http://sesame.geopsy.org/Papers/HV_User_Guidelines.pdf

Barde-Cabusson S., Finizola A., Grobbe N. (2021). A practical approach for self-potential data acquisition, processing, and visualization. Interpretation, Vol.9, No. 1, DOI:10.1190/int-2020-0012.1.

Bergmann P., Schmidt-Hattenberger C., Kiessling D., Rücker C., Labitzke T., Henninges J., Gunther B., Schütt H. (2012). Surface-downhole electrical resistivity tomography applied to monitoring of CO2 storage at Ketzin, Germany. Geophysics 77(6), B253-B267.

Bettig B., Bard P.Y., Scherbaum F., Riepl J., Cotton F., Cornou C., Hatzfeld D. (2001). Analysis of dense array noise measurements using the modified spatial autocorrelation method (SPAC): application to the Grenoble area. Boll. Geofis. Teor. Appl. 42, 281–304.

Bigi S., Beaubien S.E., Ciotoli G., D'Ambrogi C., Doglioni C., Ferrante V., Lombardi S., Milli S., Orlando L., Ruggiero L., Tartarello M.C., Sacco P. (2014). Mantle-derived CO2 migration along active faults within an extensional basin margin (Fiumicino, Rome, Italy). Tectonophysics 637, 137-149.

Bosman A., Orlando L. (2017). Bedforms on the Lowermost Reach of the Tiber River (Rome, Italy): Preliminary Results from Integrated Geophysical Surveys and Samplings. Atlas of Bedforms in the Western Mediterranean. ISBN: 978-3-319-33938-2. DOI:10.1007/978-3-319-33940-5_16.

Bosman A., Casalbore D., Anzidei M., Muccini F., Carmisciano C. (2015). The first ultra-high resolution Digital Terrain Model of the shallow-water sector around Lipari Island (Aeolian Islands, Italy). Annals of Geophysics 58(2), 2015. https://doi.org/10.4401/ag-6746.

Capon J. (1969). High-resolution frequency-wavenumber spectrum analysis Proceedings IEEE 57, 1408–1418.

Byrdina S., Revil A., Pant S. R., Koirala B. P., Shrestha P. L., Tiwari D. R., Gautam U. P., Shrestha K., Sapkota S. N., Contraires S., Perrier F. (2009). Dipolar self-potential anomaly associated with carbon dioxide and radon flux at Syabru-Bensi hot springs in central Nepal. J. Geophys. Res. 114, B10101.

Carapezza M. L., Tarchini L., Granieri D., Martelli M., Gattuso A., Pagliuca N., Ranaldi M., Ricci T., Grassa F., Rizzo A., Pizzino L., Sciarra A. (2015). Gas blowout from shallow boreholes near Fiumicino International Airport (Rome): Gas origin and hazard assessment. Chemical Geology 407, 54-65.

Carcione J. M., Gei D., Picotti S., Michelini A. (2011). Cross-hole electromagnetic and seismic modeling for CO2 detection and monitoring in a saline aquifer. Journal of Petroleum Science and Engineering 162-172.

Cardarelli E., De Donno G. (2017). Multidimensional electrical resistivity survey for bedrock detection at the Rieti Plain (Central Italy). J. Appl. Geophys. 141, 77–87. https://doi.org/https://doi.org/10.1016/j.jappgeo.2017.04.012.

Cardarelli E., De Donno G., Scatigno C., Oliveti I., Martinez M.P., Prieto-Taboada N. (2016). Geophysical and geochemical techniques to assess the origin of rising damp of a Roman building (Ostia Antica archaeological site). Microchemical Journal 129, 49-57.

Ciotoli G., Etiope G., Marra F., Florindo F., Giraudi C., Ruggiero L. (2016). Tiber delta CO2-CH4 degassing: a possible hybrid, tectonically active sediment-hosted geothermal system near Rome. Journal of Geophysical Research: Solid Earth 121(1), 48-69.

De Donno G., Cardarelli E. (2017). VEMI: a flexible interface for 3D tomographic inversion of time- and frequency-domain electrical data in EIDORS. Near Surf. Geophys. 15, 43-58.

Fleury M., Deschamps H. (2008). Electrical conductivity and viscosity of aqueous NaCl solutions with dissolved CO2. Journal of Chemical & Engineering Data 53(11), 2505-2509.

Gélis C., Revil A., Cushing M. E., Jougnot D., Lemeille F., Cabrera J., De Hoyos A., Rocher M. (2010). Potential of Electrical Resistivity Tomography to Detect Fault Zones in Limestone and Argillaceous Formations in the Experimental Platform of Tournemire, France. Pure and Applied Geophysics 167, 1405–1418.

Goebel M., Pidlisecky A., Knight R. (2017). Resistivity imaging reveals complex pattern of saltwater intrusion along Monterey coast. Journal of Hydrology 551, 746-755.

Gresse M., Vandemeulebrouck J., Byrdina S., Chiodini G., Revil A., Johnson T.C., Ricci T., Vilardo G., Mangiacapra A., Lebourg T., Grangeon J., Bascou P., Metral L. (2017). Three-dimensional electrical resistivity tomography of the Solfatara crater (Italy): Implication for the multiphase flow structure of the shallow hydrothermal system. Journal of Geophysical Research: Solid Earth 122(11), 8749-8768.

Hamilton E.L. (1979). Vp/Vs and Poisson’s ratios in marine sediments and rocks. The Journal of the Acoustical Society of America 66(4), 1093-1101.

Hansell A., Oppenheimer C. (2004). Health hazards from volcanic gases: a systematic literature review. Archives of Environmental Health: An International Journal 59(12), 628-639.

Jardani A., Revil A., Bolève A., Dupont, J.P. (2008). Three-dimensional inversion of self-potential data used to constrain the pattern of groundwater flow in geothermal fields. Journal of Geophysical Research: Solid Earth 113(B9).

Johansson S., Rosqvist H., Svensson M., Dahlin T., Leroux V. (2011). An alternative methodology for the analysis of electrical resistivity data from a soil gas study. Geophysical Journal International 186(2), 632–640, https://doi.org/10.1111/j.1365-246X.2011.05080.x

Lambert M., Schmalholz S. M., Saenger E. H., Steiner B. (2009). Low-frequency microtremor anomalies at an oil and gas field in Voitsdorf, Austria. Geophysical Prospecting 57(3), 393-411, DOI: 10.1111/j.1365-2478.2008.00734.x.

Lane J.W., White E.A., Steele G.V., Cannia J.C. (2008). Estimation of Bedrock Depth Using the Horizontal-to-Vertical (H/V) Ambient-Noise Seismic Method. Symposium on the Application of Geophysics to Engineering and Environmental Problems 490-502, DOI: 10.4133/1.2963289.

Legaz A., Revil A., Roux P., Vandemeulebrouck J., Gouédard P., Hurst T., Bolève A. (2009). Self-potential and passive seismic monitoring of hydrothermal activity: A case study at Iodine Pool, Waimangu geothermal valley, New Zealand. Journal of Volcanology and Geothermal Research 179(1-2), 11-18.

Loke M.H., Acworth I., Dahlin T. (2003). A comparison of smooth and blocky inversion methods in 2D electrical imaging surveys. Exploration Geophysics 34(3), 182-187.

Maffucci R., Ciotoli G., Pietrosante A., Cavinato G.P., Milli S., Ruggiero L., Sciarra A., Bigi S. (2022). Geological hazard assessment of the coastal area of Rome (Central Italy) from multi-source data integration. Engineering Geology 106527.

Marcucci S., Milana G., Hailemikael S., Carlucci G., Cara F., Di Giulio G., Vassallo M. (2019). The Deep Bedrock in Rome, Italy: A New Constraint Based on Passive Seismic Data Analysis. Pure and Applied Geophysics 176(6), doi: 10.1007/s00024-019-02130-6.

Milli S., D'Ambrogi C., Bellotti P., Calderoni G., Carboni M. G., Celant A., Di Bella L., Di Rita F., Frezza V., Magri D., Pichezzi R.M., Ricci V. (2013). The transition from wave-dominated estuary to wave-dominated delta: the Late Quaternary stratigraphic architecture of Tiber River deltaic succession (Italy). Sedimentary Geology 284, 159-180.

Nickschick T., Flechsig C., Meinel C., Mrlina J., Kämpf, H. (2017). Architecture and temporal variations of a terrestrial CO2 degassing site using electric resistivity tomography and self-potential. International Journal of Earth Sciences 106(8), 2915-2926.

Ohrnberger M., Schissele E., Cornou C., Bonnefoy-Claudet S., Wathelet M., Savvaidis A., Scherbaum F., Jongmanns D. (2004). Frequency wavenumber and spatial autocorrelation methods for dispersion curve determination from ambient vibration recordings, in Proceedings of the 13th World Conference on Earthquake Engineering, Vancouver, Canada, paper no. 946, available at: https://www.iitk.ac.in/nicee/wcee/article/13_946.pdf

Pischiutta M., Anselmi M., Cianfarra P., Rovelli A., Salvini, F. (2013). Directional site effects in a non-volcanic gas emission area (Mefite d'Ansanto, southern Italy): Evidence of a local transfer fault transversal to large NW–SE extensional faults?. Physics and Chemistry of the Earth, Parts A/B/C 63, 116-123.

Qian R., Liu L. (2020). Imaging the active faults with ambient noise passive seismics and its application to characterize the Huangzhuang-Gaoliying fault in Beijing Area, northern China. Engineering Geology 268, 105520, DOI: 10.1016/j.enggeo.2020.105520

Riedel M., Spence G. D., Chapman N. R., Hyndman R. D. (2002). Seismic investigations of a vent field associated with gas hydrates, offshore Vancouver Island. Journal of Geophysical Research: Solid Earth 107(B9), EPM-5.

Sanders N.R. (1997). Measuring forecast accuracy: some practical suggestions. Production and Inventory Management Journal 38(1), 43.

Sella P., Billi A., Mazzini I., De Filippis L., Pizzino L., Sciarra A., Quattrocchi F. (2014). A newly-emerged (August 2013) artificially-triggered fumarole near the Fiumicino airport, Rome, Italy. Journal of Volcanology and Geothermal Research 280, 53-66.

Souied Ahmed A., Jardani A., Revil A., Dupont J. P. (2013). SP2DINV: A 2D forward and inverse code for streaming potential problems. Computers & Geosciences 59, 9-16.

Vesnaver A., Busetti M., Baradello L. (2021). Chirp data processing for fluid flow detection at the Gulf of Trieste (northern Adriatic Sea). Bull. Geophys. Oceanogr. 62, 365-386.

Wathelet M., 2008. An improved neighborhood algorithm: parameter conditions and dynamic scaling. Geophys. Res. Lett. 35, L09301, doi:10.1029/2008GL033256.

Wathelet M., Jongmans D., Ohrnberger M., Bonnefoy-Claudet, S., 2008. Array performances for ambient vibrations on a shallow structure and consequences over Vs inversion. Journal of Seismology 12, 1–19.

Wathelet M., Chatelain J.L., Cornou C., Di Giulio G., Guillier B., Ohrnberger M., Savvaidis A. (2020). Geopsy: A User-Friendly Open-Source Tool Set for Ambient Vibration Processing. Seismological Research Letters 91(3), 1878-1889. doi: 10.1785/0220190360.

Zlotnicki J., Nishida Y. (2003). Review on morphological insights of self-potential anomalies on volcanoes. Surveys in Geophysics 24(4), 291-338.